



Nano-Au/CeO₂ catalysts for CO oxidation: Influence of dopants (Fe, La and Zr) on the physicochemical properties and catalytic activity



Putla Sudarsanam ^a, Baithy Mallesham ^a, Padigapati S. Reddy ^a, D. Großmann ^b, Wolfgang Grünert ^b, Benjaram M. Reddy ^{a,*}

^a Inorganic and Physical Chemistry Division, CSIR – Indian Institute of Chemical Technology, Uppal Road, Hyderabad 500 607, India

^b Laboratory of Industrial Chemistry, Ruhr-University Bochum, D-44780 Bochum, Germany

ARTICLE INFO

Article history:

Received 15 June 2013

Received in revised form 12 August 2013

Accepted 19 August 2013

Available online 29 August 2013

Keywords:

Nano-gold

Ceria

Ceria-zirconia

CO oxidation

Carbonate species

ABSTRACT

The present investigation was undertaken to know the influence of different dopants on the physicochemical properties and catalytic behavior of nano-Au/CeO₂ catalyst for CO oxidation. Accordingly, various metal ions namely, Fe³⁺, La³⁺ and Zr⁴⁺ were incorporated into the ceria lattice by a facile coprecipitation approach using ultra-high dilute aqueous solutions. An anion adsorption method was used to prepare the Au/doped-CeO₂ catalysts in the absence of any base, reducing and protective agents. The physicochemical characterization was performed by XRD, BET surface area, ICP-AES, TG-DTA, FT-IR, TEM, UV-vis DRS, Raman, XPS and TPD techniques. Doped CeO₂ exhibited smaller crystallite size, higher BET surface area and larger amount of oxygen vacancies than the pure CeO₂. These remarkable properties showed a beneficial effect toward gold particle size as confirmed by XRD and TEM studies. XPS results revealed that Au is present in the metallic state and Ce in both +3 and +4 oxidation states. Incorporation of Zr into the Au/CeO₂ resulted in high CO oxidation activity attributed to the presence of more Ce³⁺ ions and oxygen vacancies. In contrast, the La-incorporation caused an opposite effect due to the presence of carbonate species on the surface of Au/CeO₂–La₂O₃ catalyst, which blocked the active sites essential for CO oxidation. It was shown that accumulation of carbonate species strongly depends on the acid-base properties of the supports. The catalytic performance of Au catalysts is highly dependent on the nature of the support.

© 2013 Elsevier B.V. All rights reserved.

1. Introduction

Since the pioneering research of Haruta et al. the use of supported gold nanoparticles (Au NPs) for low temperature CO oxidation has attracted significant interest in heterogeneous catalysis [1]. CO is a highly toxic gas and exposure to a few hundred ppm can cause permanent health damage or even death [2,3]. The study of CO oxidation over Au catalysts provided several industrial applications, such as gas purification in CO₂ lasers and CO gas sensors, air-purification devices for respiratory protection, and pollution control devices for reducing automotive emissions [4,5]. The additional potential uses of Au catalysts have been actively investigated, including water-gas-shift reaction, NO_x abatement, combustion of volatile organic compounds, selective oxidation and hydrogenation of organic compounds, C–C coupling reactions, and synthesis of N- and O-heterocycles [5,6].

Numerous factors have been examined, including the Au particle size and its size distribution, Au oxidation state, nature of the

support and the preparation method to elucidate such exceptional low temperature CO oxidation activity of Au catalysts [7,8]. Primarily, the nature of the metal oxide supports and thereby, stimulated interactions between gold and metal oxides play a significant role in the CO oxidation. The key function of any support is to prevent abnormal growth of active metal particles. The enhanced interactions between the gold and metal oxides can effectively stabilize the gold particles through a wider contact area, hence higher perimeter interfaces around them. They also facilitate additional active sites at the gold/support interface for the adsorption of the reactants close to the gold particles [9,10]. Au NPs have been deposited on a variety of metal oxides, such as CeO₂, La₂O₃, Fe₂O₃ and TiO₂ (active supports), and Al₂O₃, SiO₂ and MgO (inert supports) [11,12]. It was found that Au catalysts show remarkable activity when the Au NPs are dispersed on the active metal oxide supports. The difference between inert and active supports can be assigned to their adsorption ability of O₂ in the CO oxidation. An inert oxide exhibits poor O₂ adsorption capacity and the oxidation of CO proceeds by dissociative adsorption of O₂ on the gold. In such case, the activity behavior is favored either on metal surface defect sites (e.g., edge, kink, or step) or on small gold particles. In contrast, an active oxide has strong ability to adsorb O₂ where it may or may not

* Corresponding author. Tel.: +91 40 2719 1714; fax: +91 40 2716 0921.

E-mail addresses: bmreddy@iict.res.in, mreddyb@yahoo.com (B.M. Reddy).

dissociate before reacting with CO adsorbed on the gold. At this juncture, CO oxidation is sensitive to the microcrystalline structure of the gold-support interface.

Among the metal oxide supports, CeO₂ has gained remarkable attention due to the presence of oxygen vacancy defects generated by Ce⁴⁺/Ce³⁺ redox process, which allows effective O₂ adsorption and activation for CO oxidation [7]. It is a well-established fact in the literature that doping of appropriate metal ions into the ceria lattice enhance its unique structural and redox properties [13,14]. Doped ceria materials exhibit smaller crystallite size, higher surface area, abundant oxygen vacancies and enhanced redox properties compared to the parent ceria. The choice of dopant metal ion and its amount to incorporate into the ceria are very crucial because different dopants will have different optimum compositions and some are even not miscible over the full composition range. For example, 50% Zr-incorporation into the CeO₂ resulted in better redox properties compared to other molar ratios [15,16]. When Zr⁴⁺ is incorporated into the CeO₂ lattice, the induced distortion of the O²⁻ sublattice in the mixed oxide enhances the mobility of lattice oxygen [17]. Thus, the reducible nature of Ce⁴⁺ is no longer confined to the ceria surface, but it extends intensely into the bulk, promoting the reduction of Ce⁴⁺ to Ce³⁺. In contrast, the Ce-La mixed oxides even at low doping amount of La (e.g., 20% in balance with Ce) exhibit a large amount of oxygen vacancies and improved redox properties accounting for the charge neutrality in the ceria lattice [14]. On the other hand, the solubility of Fe in the CeO₂ is very low, and better physicochemical properties are observed for small doping amounts of Fe, in particular for 10% of Fe-incorporation [18–20]. Therefore, the amount of metal ions to incorporate into the ceria lattice highly depends on the nature of the metal.

The objective of the present study was to investigate the effect of dopants on the physicochemical properties and catalytic behavior of nano-Au/CeO₂ catalyst for CO oxidation. Accordingly, we have prepared a series of CeO₂-based supports by incorporating the optimum amounts of Zr, Fe and La into the ceria lattice. Generally, metal oxide supported Au catalysts are prepared by conventional deposition-precipitation or coprecipitation methods [21]. In these processes, the Au precursor is precipitated by means of a base (NaOH, (NH₄)₂CO₃, etc.) under normalized pH conditions. Although, these techniques have proven to produce small Au particles, control over the particle dispersion is rather difficult. Herein, an anion adsorption method was used to prepare the Au/doped-CeO₂ catalysts in the optimism of improving the Au dispersion [21]. For comparison, an undoped Au/CeO₂ catalyst was also prepared under identical conditions. The synthesized catalysts were systematically characterized by means of various techniques, namely, X-ray diffraction (XRD), BET surface area, inductively coupled plasma atomic emission spectroscopy (ICP-AES), X-ray photoelectron spectroscopy (XPS), Raman spectroscopy, UV-vis diffuse reflectance spectroscopy (UV-vis DRS), thermogravimetric-differential thermal analysis (TG-DTA), Fourier transform infrared (FT-IR) spectroscopy, temperature programmed desorption (TPD) and transmission electron microscopy (TEM). The catalytic performance was studied for the oxidation of CO in a fixed bed micro-reactor. Attempts were made to correlate the catalytic activity results with the characterization studies.

2. Experimental

2.1. Catalyst preparation

The ceria-based mixed oxide supports, namely, CeO₂-M_xO_y (M_xO_y = Fe₂O₃, La₂O₃ and ZrO₂) were prepared by a facile and economical coprecipitation method from ultra-high

dilute aqueous solutions. The precursors employed were NH₄Ce(NO₃)₃·6H₂O (Aldrich, AR grade), ZrO(NO₃)₂·xH₂O (Fluka, AR grade), La(NO₃)₃·6H₂O (Aldrich, AR grade) and Fe(NO₃)₃·9H₂O (Aldrich, AR grade). In a typical procedure, to prepare CeO₂-Fe₂O₃ (CF = 90:10 molar ratio based on metal oxides) the required quantities of metal precursors were dissolved in double distilled water separately under mild stirring conditions and mixed together. Then, an aqueous NH₃ solution was added drop-wise until the pH of the solution reached to ~8.5. The produced precipitates were recovered by filtration and washed with double distilled water several times until free from anion impurities, oven-dried at 393 K for 12 h and finally calcined in air at 773 K for 5 h (5 K/min). Similarly, CeO₂-ZrO₂ (CZ = 50:50), CeO₂-La₂O₃ (CL = 80:20), and a pure CeO₂ (C) were also prepared by adopting the same procedure under identical conditions.

A simple and efficient anion adsorption method was used to prepare 1 wt.% Au/doped-CeO₂ catalysts in the absence of any base, reducing and protective agents [10,22]. In brief, an appropriate amount of HAuCl₄·4H₂O (Alfa Aesar, 99.9%) was dissolved in deionized water and then, the gold solution was heated to 343 K followed by the addition of required amount of support. After stirring for 1 h, the solution was cooled to room temperature, filtered off, washed with aq. NH₃ and distilled water in order to remove Cl⁻ ions and oven dried at 373 K for 12 h. Finally, the samples were calcined in air at 573 K for 4 h (1 K/min) and stored in a desiccator under vacuum conditions. The Au/CeO₂ sample was also synthesized under identical conditions for the purpose of comparison. For convenience, the prepared catalysts, namely, Au/CeO₂, Au/CeO₂-Fe₂O₃, Au/CeO₂-La₂O₃ and Au/CeO₂-ZrO₂ are designated as AC, ACF, ACL and ACZ, respectively.

2.2. Catalyst characterization

The synthesized catalysts were analyzed by X-ray diffraction using a Rigaku Multiflex instrument equipped with nickel-filtered Cu K α (0.15418 nm) radiation source and a scintillation counter detector. The intensity data were collected over a 2 θ range of 12–80° with a 0.02° step size and using a counting time of 1 s per point. The average crystallite size of the samples was estimated with the help of Scherrer equation and the lattice parameter was calculated by a standard cubic indexation method. Specific surface areas of the samples were determined by single point BET analysis of the nitrogen adsorption isotherms at liquid N₂ temperature (77 K) recorded on a SMART SORB-92/93 instrument via a thermal conductivity detector (TCD). Prior to the experiment, samples were degassed at 393 K for 2 h to remove any surface adsorbed residual moisture. Surface area was obtained by using desorption data.

Raman spectra were recorded at room temperature using a LabRam HR800UV Raman spectrometer (Horiba Jobin-Yvon) fitted with a confocal microscope and liquid-nitrogen cooled charge-coupled device (CCD) detector. Samples were excited with the emission line at 632.81 nm from an Ar⁺ ion laser (Spectra Physics) which was focused on the sample under the microscope with the diameter of the analyzed spot being ~1 μ m. The acquisition time was adjusted according to the intensity of Raman scattering. The X-ray photoelectron spectroscopy analysis was performed on a VG Scientific ESCALAB-210 spectrometer using Mg K α radiation (1253.6 eV) from an X-ray source operating at 15 kV and 20 mA. The spectra were collected with an analyzer pass energy of 20 eV, 0.1 eV step and an electron take off angle of 90°. The recorded XPS spectra were charge corrected with respect to the C 1s peak at 284.6 eV. The samples were pressed into thin wafers and degassed in a preparation chamber before analysis. The Shirley background subtraction and peak fitting with Gaussian-Lorentzian product peak was performed using XPS processing program Advantage (Thermo Electron Corporation).

TEM studies were made on a JEM-2010 (JEOL) instrument equipped with a slow-scan CCD camera at an accelerating voltage of 200 kV. Samples for TEM were prepared by crushing the materials in an agate mortar and dispersing them ultrasonically in ethyl alcohol. After dispersion, a droplet was deposited on a copper grid supporting a perforated carbon film and allowed to dry. The specimen was examined under vacuum at room temperature. The UV-vis DRS measurements were performed over the wavelength range of $\lambda = 200\text{--}750\text{ nm}$ using a GBS-Cintra 10e UV-vis NIR spectrophotometer with an integration sphere diffuse reflectance attachment. Sample was diluted in a KBr matrix by pelletization.

FT-IR spectra were recorded on a Nicolet 740 FT-IR spectrometer at ambient conditions using KBr discs with a nominal resolution of 4 cm^{-1} and averaging 100 spectra. TG-DTA analysis was performed on a Mettler Toledo TG-SDTA instrument. The samples were heated from ambient temperature to 1073 K under the flow of N_2 . The heating rate in each case was kept at 10 K/min. The TPD (NH_3/CO_2 -TPD) measurements were performed on a Micromeritics AutoChem 2910 instrument. A thermal conductivity detector was used for continuous monitoring of the desorbed gas and the areas under the peaks were integrated. Prior to TPD measurements, samples were pre-treated at 573 K for 1 h and then saturated with ultra-pure anhydrous NH_3/CO_2 for 1 h, and subsequently flushed with He gas to remove the physisorbed gas.

2.3. Catalytic activity measurement

The catalytic activity of the supported gold samples for CO oxidation was measured at atmospheric pressure in the temperature range of 223–573 K in a fixed bed quartz micro-reactor. The reaction was performed by using 1% CO and 20% O_2 balanced with He gas. Using mass-flow controllers, 100 ml/min of the feed were dosed onto 100 mg of sample (250–355 μm sieve fraction), which results in $\text{W/F} = 0.06\text{ g s ml}^{-1}$. The reaction temperature was monitored using a thermocouple placed in the hollow part of the reactor. All gas concentrations were monitored with a X-STREAM X2GP gas analyzer (Emerson), which applies non-dispersive IR photometry for CO and CO_2 and a magnetic method for O_2 . Prior to oxidation of CO, the catalyst was heated to 573 K in 20% O_2 balanced by the He gas using a heating ramp of 1 K/min and kept at the final temperature for 1 h.

3. Results and discussion

3.1. Catalyst characterization

The XRD profiles of ceria-based supports investigated in the present study are shown in Fig. 1. As can be seen from the figure, all ceria-based supports clearly show the fluorite-type cubic structure of CeO_2 [13,14,23,24]. Conversely, no XRD peaks related to dopant metal oxides, namely, Fe_2O_3 , La_2O_3 and ZrO_2 were observed. Interestingly, the diffraction peaks of doped ceria are broad with 2-theta values shifted to various extents in comparison to pure ceria. These noteworthy observations demonstrate the existence of smaller crystallite sizes in the doped ceria supports exhibiting either lattice contraction or expansion. The diffraction peaks of CZ and CF samples were shifted to higher angle side relative to C, whereas the CL patterns are shifted to lower angle side. Shift in the peak positions could be elucidated by comparing the ionic radii of guest ($\text{Fe}^{3+} \sim 0.064\text{ nm}$, $\text{Zr}^{4+} \sim 0.084\text{ nm}$ and $\text{La}^{3+} \sim 0.11\text{ nm}$) and host ions ($\text{Ce}^{4+} \sim 0.097\text{ nm}$). Perceptibly, the ionic radius of La^{3+} is high compared to the Ce^{4+} , hence lattice expansion is noticed for CL support due to the incorporation of La^{3+} into the CeO_2 lattice. On the contrary, lattice contraction is found for CZ and CF samples attributed to the substitution of Ce^{4+} by smaller sized Zr^{4+} and Fe^{3+} cations, respectively.

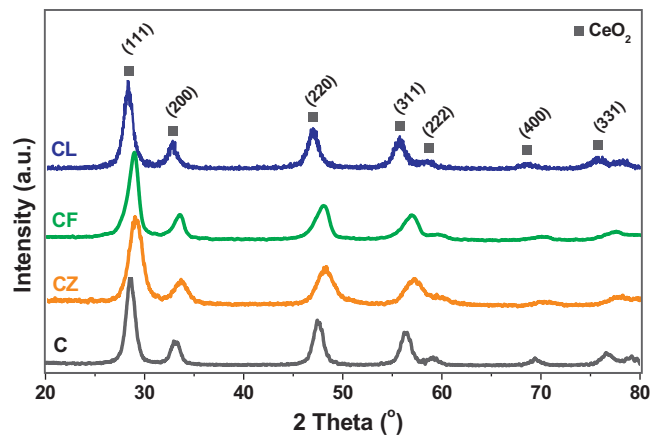


Fig. 1. XRD patterns of CeO_2 (C), $\text{CeO}_2\text{-ZrO}_2$ (CZ), $\text{CeO}_2\text{-Fe}_2\text{O}_3$ (CF) and $\text{CeO}_2\text{-La}_2\text{O}_3$ (CL) supports.

Accordingly, a decrease in the lattice parameters is noted for CZ and CF supports in comparison to pure CeO_2 , whereas the CL sample showed an increased lattice parameter (Table 1). The observed key features, such as peak shift, variation in the lattice parameter and absence of XRD peaks pertaining to the dopant metal oxides evidently confirm the formation of ceria solid solutions.

In order to know the influence of dopants on the textural properties of ceria, average crystallite sizes and specific surface areas were determined (Table 1). Remarkably, the addition of dopants led to a decrease in the crystallite size of ceria, indicating the favorable role of dopants toward inhibition of crystal growth of ceria against high thermal treatments. The average crystallite size of C, CL, CF and CZ samples are 8.9, 8.3, 6.7 and 4.7 nm, respectively. In general, the mixed oxides exhibit higher BET surface areas in comparison to the individual oxides [24]. As asserted, the surface area of ceria was significantly increased after incorporation of metal ions, in particular in the case of Zr-incorporation. The specific surface area of C, CL, CF and CZ samples are 41, 66, 72 and $84\text{ m}^2/\text{g}$, respectively, which corroborates well with the crystallite size decrease (Table 1). The meticulous correlation of crystallite size and surface area of ceria supports reveals that Zr^{4+} -incorporation into the CeO_2 reduces its crystallite size and enhances its surface area compared to other metal ions (Fig. S1 of the supplementary material).

Raman spectroscopy is an excellent technique to investigate the structural properties of ceria-based materials because of its strong sensitive nature to both M–O bond arrangement and lattice defects [25]. Fig. 2 represents Raman spectra of ceria-based mixed oxides along with pure ceria. Pure CeO_2 shows a prominent peak at $\sim 460\text{ cm}^{-1}$, which could be assigned to F_{2g} Raman-active mode of the fluorite structured CeO_2 , confirming the observations made from the XRD studies [18]. An additional small shoulder at around 600 cm^{-1} denotes the oxygen vacancy defects (O_v) preferentially located on the surface of CeO_2 (Fig. 2, inset). Intriguingly, the F_{2g} band of CZ is shifted to higher wavenumber side ($\sim 474\text{ cm}^{-1}$; Zr), whereas the F_{2g} bands of CL and CF supports are shifted to lower

Table 1

BET surface area, average crystallite size, and lattice parameter of CeO_2 (C), $\text{CeO}_2\text{-La}_2\text{O}_3$ (CL), $\text{CeO}_2\text{-Fe}_2\text{O}_3$ (CF) and $\text{CeO}_2\text{-ZrO}_2$ (CZ) supports.

| Sample | BET surface area (m^2/g) | CeO_2 lattice parameter (\AA) ^a | CeO_2 crystallite size (nm) ^b |
|--------|--|--|---|
| C | 41 | 5.410 | 8.9 |
| CL | 66 | 5.488 | 8.3 |
| CF | 72 | 5.358 | 6.7 |
| CZ | 84 | 5.350 | 4.7 |

^{a,b}Estimated from XRD studies.

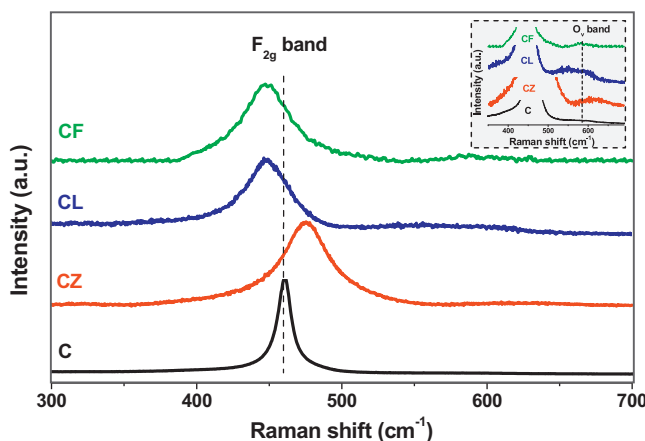


Fig. 2. Vis-Raman spectra of CeO₂ (C), CeO₂-ZrO₂ (CZ), CeO₂-La₂O₃ (CL) and CeO₂-Fe₂O₃ (CF) supports.

wavenumbers ($\sim 447\text{ cm}^{-1}$; La and $\sim 448\text{ cm}^{-1}$; Fe) relative to pure CeO₂. The shift in the F_{2g} mode reveals the variation of the M-O vibration frequency, which is attributed to the difference in the ionic radii of Ce⁴⁺ and dopants [25]. No Raman bands corresponding to ZrO₂, Fe₂O₃ and La₂O₃ were found, confirming the formation of ceria-based solid solutions and corroborating well with the XRD results. Further, the incorporation of metal ions into the ceria enhances the oxygen vacancies (Fig. 2, inset). The CZ and CF samples exhibited only one type of O_v band at $\sim 600\text{ cm}^{-1}$, whereas the CL sample displayed two bands at ~ 553 and $\sim 601\text{ cm}^{-1}$. The peak at lower wavenumber reveals the extrinsic oxygen vacancies and the higher wavenumber band indicates the intrinsic oxygen vacancies [25,26]. Generally, the intrinsic vacancies could be formed due to the presence of Ce³⁺ ions, while extrinsic vacancies are generated by the charge compensation effect of lower valence dopants. Therefore, the Zr⁴⁺-incorporation promotes only intrinsic vacancies attributed to the presence of Ce³⁺ ions in the CZ sample (evidence from XPS studies, Fig. 6). For CL support, both extrinsic and intrinsic vacancies were found, which can be ascribed to doping of lower valence La³⁺ as well as the existence of Ce³⁺ ions, respectively. In contrast to CL, the CF sample showed only one O_v band. It was suggested that small doping amounts of Fe³⁺ induces the generation of oxygen vacancies (vacancy compensation mechanism), whereas large doping amounts annihilate them (dopant interstitial compensation mechanism) [27]. In the present study, due to low doping amounts of Fe³⁺, substantial concentration of oxygen vacancies were observed.

Fig. 3 represents the XRD patterns of supported gold catalysts calcined at 573 K. A close examination of Figs. 1 and 3 reveals that there was no discernible variation in the diffraction profiles of ceria-based supports after deposition of gold. This notable result suggests the preservation of crystalline structure and average crystallite sizes of ceria in the Au-containing samples [28]. A broad XRD (111) peak at $2\theta \sim 38.18^\circ$ was noticed for AC sample due to the face centered cubic structure of gold (Fig. 3, inset), indicating the presence of larger Au particles [12]. In contrast, no Au diffraction peaks were found in the case of ACZ, ACL and ACF catalysts owing to the fact that the gold particle sizes are very small (<5 nm) [29]. The absence of Au diffraction peaks also indicates the existence of highly dispersed gold particles on the surface of doped ceria supports that are too small to be detected by the XRD technique [29,30]. Table 2 summarizes the gold loading and BET surface areas of the supported gold samples. The ICP-AES measurements showed that the employed anion adsorption method provide better gold retention efficiencies as observed in the traditional deposition-precipitation techniques [18,30]. The determined gold contents of AC, ACZ, ACL and ACF

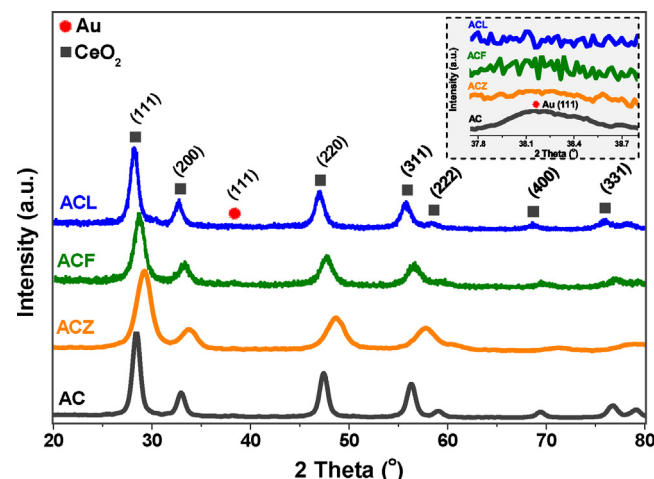


Fig. 3. XRD patterns of Au/CeO₂ (AC), Au/CeO₂-ZrO₂ (ACZ), Au/CeO₂-Fe₂O₃ (ACF) and Au/CeO₂-La₂O₃ (ACL) catalysts.

samples were 0.89, 0.94, 0.98 and 0.76 wt.%, respectively. Moreover, the chlorine content is very low for all the gold catalysts (<200 ppm). The ammonia treatment would be the crucial factor in the efficient removal of chlorine residues [10,22]. The obtained atomic ratios of host to guest ions (Ce/Zr = 0.47/0.53, Ce/La = 0.78/0.22 and Ce/Fe = 0.89/0.11) are close to the calculated values (Ce/Zr = 0.5/0.5, Ce/La = 0.8/0.2 and Ce/Fe = 0.9/0.1), confirming the stoichiometric atomic concentration. The determined specific surface areas of AC, ACZ, ACL and ACF catalysts are 38, 73, 54 and 61 m²/g, respectively. The decrease in the surface area of ceria supports after the addition of gold might be due to the penetration of the dispersed gold into the pores of the support.

XPS analysis was performed to know the valence states of the elements present in the prepared catalysts. The Au 4f XPS profiles of gold catalysts are illustrated in Fig. 4. The Au 4f spectra are characterized by a doublet corresponding to Au 4f_{7/2} and Au 4f_{5/2} states with a separation of about 3.7 eV. All the catalysts showed a main Au 4f_{7/2} peak in the range of 83.3–83.6 eV with the analogous Au 4f_{5/2} peak at around 87.1–87.4 eV, which obviously confirm the presence of metallic gold (Au⁰) species [31,32]. On the other hand, XPS peaks related to oxidized gold (Au¹⁺ 4f_{7/2} at 84.5 eV and Au³⁺ 4f_{7/2} at 86.6 eV) were not identified. However, the quantitative assessment of the gold oxidation state by XPS technique is limited because the final state effects associated with particle size could extremely disturb the XPS features of gold [31,33]. As well, the exposure of gold particles to photoelectrons under high vacuum conditions might also affect the gold oxidation state. The O 1s XPS profiles of the gold catalysts are presented in Fig. 5. The O 1s spectra can be fitted into two peaks, indicating the existence of different oxygen species. The peak at lower binding energy ($\sim 529\text{ eV}$) reveals the lattice oxygen, whereas the peak at higher binding energy ($\sim 532\text{ eV}$) shows the surface carbonates and hydroxyl species. The analysis of the FT-IR spectra also evidenced the presence of surface

Table 2

Gold loading, gold particle size, and BET surface area of Au/CeO₂ (AC), Au/CeO₂-La₂O₃ (ACL), Au/CeO₂-Fe₂O₃ (ACF) and Au/CeO₂-ZrO₂ (ACZ) catalysts.

| Sample | Au loading (wt.%) ^a | Au particle size (nm) | BET surface area (m ² /g) |
|--------|--------------------------------|-----------------------|--------------------------------------|
| AC | 0.89 | 7.4 ^b | 38 |
| ACL | 0.98 | n.d | 54 |
| ACF | 0.76 | n.d | 61 |
| ACZ | 0.94 | 3.3 ^b | 73 |

^a Obtained from ICP-AES measurements.

^b Determined from TEM pictures.

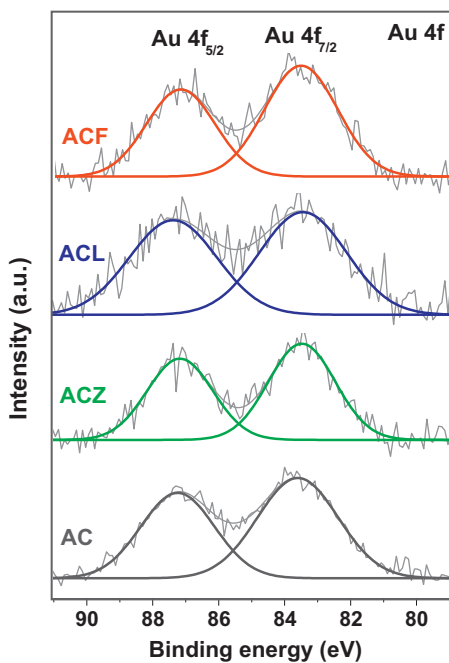


Fig. 4. Au 4f XP spectra of Au/CeO₂ (AC), Au/CeO₂–ZrO₂ (ACZ), Au/CeO₂–Fe₂O₃ (ACF) and Au/CeO₂–La₂O₃ (ACL) catalysts.

carbonates and hydroxyl species in the prepared catalysts (Fig. S2 of the supplementary material) [34,35].

The Ce 3d XP spectra of ceria-based mixed oxide supported gold catalysts are shown in Fig. 6. As can be seen from the figure, the Ce 3d XP spectra are complex in the range of 880–920 eV due to the hybridization of the O 2p valence band with the Ce 4f level in the final state of photoionization [23,24,36]. The labels u and v refer to the 3d_{3/2} and 3d_{5/2} spin-orbit components, respectively. The peaks denoted by u₀, v₀, u' and v' are characteristic peaks of Ce³⁺ ions (one main line and one satellite), whereas those marked by v, u, v'', u''' and v''' are of Ce⁴⁺ ions (one main line and two

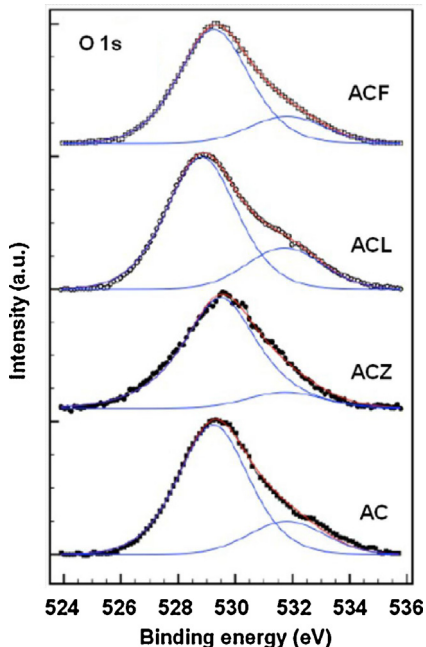


Fig. 5. O 1s XP spectra of Au/CeO₂ (AC), Au/CeO₂–Fe₂O₃ (ACF), Au/CeO₂–La₂O₃ (ACL) and Au/CeO₂–ZrO₂ (ACZ) catalysts.

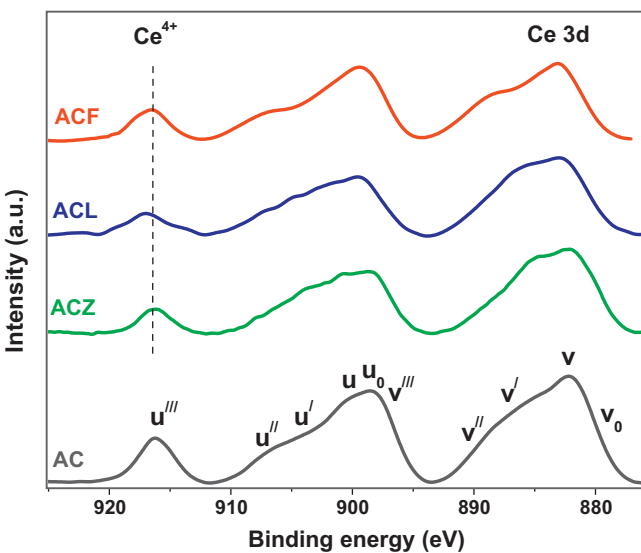


Fig. 6. Ce 3d XP spectra of Au/CeO₂ (AC), Au/CeO₂–Fe₂O₃ (ACF), Au/CeO₂–La₂O₃ (ACL) and Au/CeO₂–ZrO₂ (ACZ) catalysts.

satellites). Therefore, it can be inferred that all samples exhibit both Ce⁴⁺ and Ce³⁺ ions. The analysis of the u'''/(Ce⁴⁺) peak is one of the most convenient features to estimate the Ce reduction, because it does not overlap with any other peaks. The intensity ratio of the u''' peak to the total area of Ce 3d peak ($I_{u'''}/I_{\text{Total}}$) is used to determine the surface concentration of Ce³⁺ ions in such a way that a smaller ratio indicates a higher Ce³⁺ concentration [23,37]. The estimated $I_{u''''}/I_{\text{Total}}$ values were found to be 0.0896, 0.0876, 0.0713 and 0.0625 for AC, ACF, ACL and ACZ catalysts, respectively. Clearly, the Zr-incorporation resulted in high concentration of Ce³⁺ ions, which play a key role in CO oxidation as discussed in the later paragraphs. Furthermore, the deposition of gold also enhances the Ce³⁺ concentration along with the formation of uncoordinated sites near the very small gold particles ($d \leq 1$ nm) [38].

The Zr 3d, Fe 2p and La 3d XP spectra of the respective Au/doped-CeO₂ catalysts are investigated to know the oxidation states of the incorporated metal ions (Fig. S3 of the supplementary material). The deconvoluted peaks at around 184.8 (Zr 3d_{3/2}) and 182.2 eV (Zr 3d_{5/2}) in the Zr 3d spectrum reveal the presence of Zr⁴⁺ ions [31]. The La 3d spectrum shows two main peaks at ~834.46 (3d_{5/2}) and 851.32 eV (3d_{3/2}), which demonstrate the existence of La³⁺ ions [14]. The satellite peaks appearing on the higher energy side of the 3d_{5/2} and 3d_{3/2} peaks resulted from the core-hole screening by nearly degenerate O 2p and empty La 4f states. The general explanation for high binding energy satellite peaks is the charge transformation from O 2p to the empty 4f state of La leading to the 3d⁹ 4f¹ final states [39]. The XPS peaks of Fe 2p_{3/2} (~711 eV) and Fe 2p_{1/2} (~724.6 eV) indicate the presence of Fe³⁺ ions in the ACF sample [40]. The observed satellite peak at around 718.8 eV does not overlap with either Fe 2p_{3/2} or Fe 2p_{1/2} peaks. In addition, there is another satellite peak at ~733 eV, which is a satellite peak of the Fe 2p_{1/2}.

TEM analysis was performed to know the Au particle size of the AC and ACZ samples (Fig. S4 of the supplementary material). It must be emphasized here that the identification of gold particles from TEM images of Au/CeO₂ catalysts is hardly noticeable due to the poor contrast between Au and CeO₂ [9,28,41]. The TEM analysis of AC sample reveals larger sized gold nanoparticles with mean diameter of 7.4 nm. For ACZ sample, the observed Au nanoparticles have diameters as low as 1 nm with a mean particle size of ~3.3 nm. The presence of smaller gold nanoparticles in the ACZ sample certainly reveals the favorable role of dopant (Zr) toward the gold

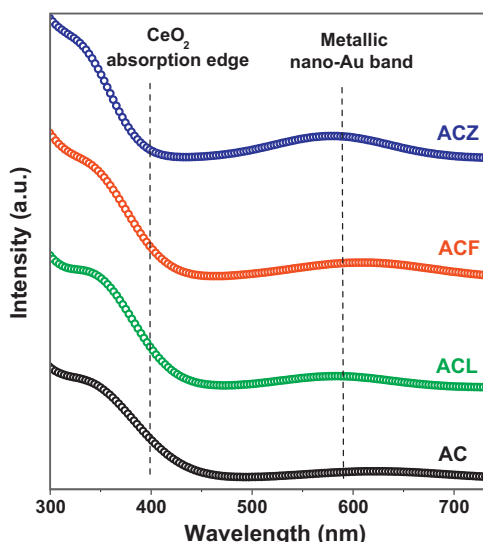


Fig. 7. UV-vis DR spectra of Au/CeO_2 (AC), $\text{Au}/\text{CeO}_2-\text{La}_2\text{O}_3$ (ACL), $\text{Au}/\text{CeO}_2-\text{Fe}_2\text{O}_3$ (ACF) and $\text{Au}/\text{CeO}_2-\text{ZrO}_2$ (ACZ) catalysts.

particle size. As we stated earlier, no Au XRD peaks were found in the case of Au/doped- CeO_2 catalysts attributed to existence of smaller gold nanoparticles (Fig. 3, inset). Therefore, by comparing the TEM analysis of ACZ and XRD results of Au/doped- CeO_2 catalysts, it can be expected that the ACL and ACF samples also exhibit smaller gold nanoparticles compared to the AC catalyst. Fig. 7 shows the UV-vis DR spectra of the Au catalysts. All samples exhibited a visible band in the range of 500–700 nm, which can be assigned to the surface plasmon resonance (SPR) of metallic gold (Au^0) nanoparticles [42–44]. The presence of Au^0 species in the prepared catalysts was also evidenced by the XPS results [44]. The appearance of the SPR band normally depends on various parameters, such as gold particle size, its shape, gold content and electronic properties of the surrounding environment [45]. On the other hand, UV-vis DRS spectroscopy is also useful to know the effect of dopants on the ceria crystallite size. Pure crystalline ceria has a band gap of 3.1 eV and absorbs strongly in the UV region with the absorption threshold near 400 nm [23]. The charge-transfer transitions between O 2p and Ce 4f levels are accountable for the UV absorption of ceria. The UV absorption edge wavelength is highly sensitive to the particle size of semiconductor materials, such as ceria and zirconia [46]. When crystallite size is below 10 nm, the band gap energy increases with decreasing the crystallite size and the UV absorption edge of the inter band transition can be blue-shifted. As can be seen from Fig. 7, the absorption edge of the inter band transition is blue-shifted from AC → ACL → ACF → ACZ, which corroborates well with the average crystallite size of the ceria supports determined from the XRD studies (Table 1). Hence, it can be suggested that incorporation of metal ions into the ceria enhances its band gap energy and reduces its crystallite size.

3.2. Catalytic CO oxidation

The catalytic activity of the gold samples was studied for CO oxidation reaction and the obtained results are presented in Fig. 8. It was found that the conversion of CO increases with reaction temperature for all the catalysts. The shapes of the activity curves clearly revealed that the AC, ACF and ACZ samples catalyze CO oxidation at lower temperatures, whereas ACL catalyst shows an opposite effect. For better comparison of the activities, we determined the reaction rates normalized to Au content at 330 K as shown in Fig. 9. The obtained values are 0.0392×10^{-6} ,

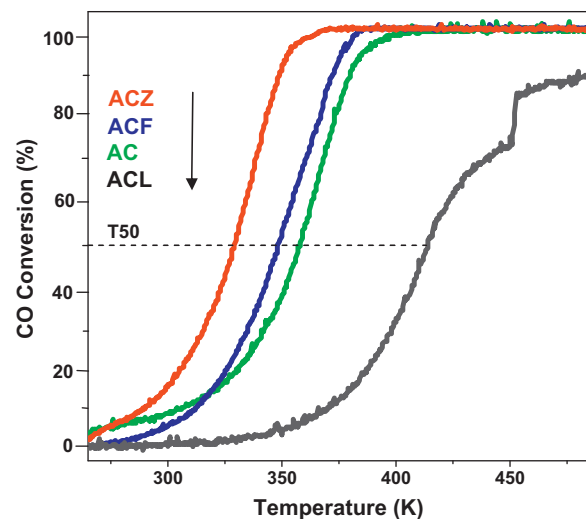


Fig. 8. Oxidation of CO over Au/CeO_2 (AC), $\text{Au}/\text{CeO}_2-\text{Fe}_2\text{O}_3$ (ACF), $\text{Au}/\text{CeO}_2-\text{La}_2\text{O}_3$ (ACL) and $\text{Au}/\text{CeO}_2-\text{ZrO}_2$ (ACZ) catalysts.

0.0152×10^{-6} , 0.00176×10^{-6} and $0.00176 \times 10^{-6} \text{ mol}_{\text{CO}} \text{ s}^{-1} \text{ g}_{\text{Au}}^{-1}$ for ACZ, ACF, AC and ACL catalysts, respectively. Several studies have shown that the CO oxidation of Au/CeO_2 catalysts follows mostly the Mars-van Krevelen type mechanism, in which CO_2 desorption determines the rate of CO oxidation [47–49]. The low reaction rate of ACL sample could be due to low CO_2 desorption from the sample surface, attributed to its strong adsorption ability toward CO_2 , as discussed in the later paragraphs. Also, the ACZ catalyst oxidizes 50% of CO (T50) at lower temperature (328 K) than the other catalysts, and the T50 values for ACF, AC and ACL catalysts are 346, 357 and 413 K, respectively. Further, the ACZ catalyst showed 100% CO conversion at around 354 K followed by ACF, AC and ACL catalysts at 376, 385 and 538 K, respectively. Surprisingly, a sharp increase in the CO oxidation after 450 K was noticed for ACL sample. The stability of the catalytic activity was studied with AC, ACF and ACZ catalysts at 328 K for 8 h (Fig. 10). It was found that both ACZ and ACF catalysts show reasonably stable CO oxidation activity, whereas the CO conversion continuously decreased with time in the case of AC catalyst.

Plausible reasons to explain the activity of gold catalysts investigated in the present work have been sought. For gold catalyzed CO oxidation, a noticeable relationship between the activity and gold particle size has been demonstrated [50]. Particularly, Au

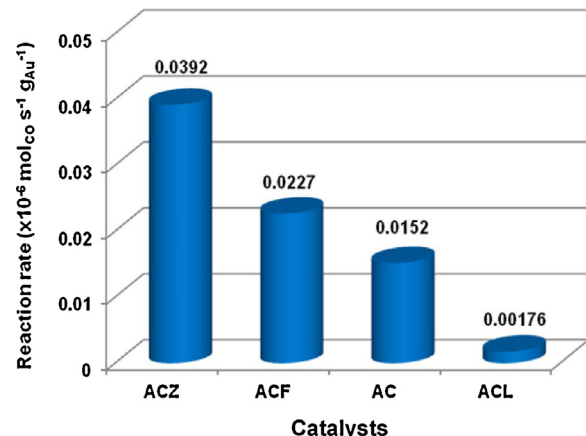


Fig. 9. Comparison of CO oxidation reaction rates at $T=330\text{ K}$ of Au/CeO_2 (AC), $\text{Au}/\text{CeO}_2-\text{Fe}_2\text{O}_3$ (ACF), $\text{Au}/\text{CeO}_2-\text{La}_2\text{O}_3$ (ACL) and $\text{Au}/\text{CeO}_2-\text{ZrO}_2$ (ACZ) catalysts. Rates were measured with 1% CO and 20% O_2 (balance – He) at $W/F=0.06\text{ g s ml}^{-1}$.

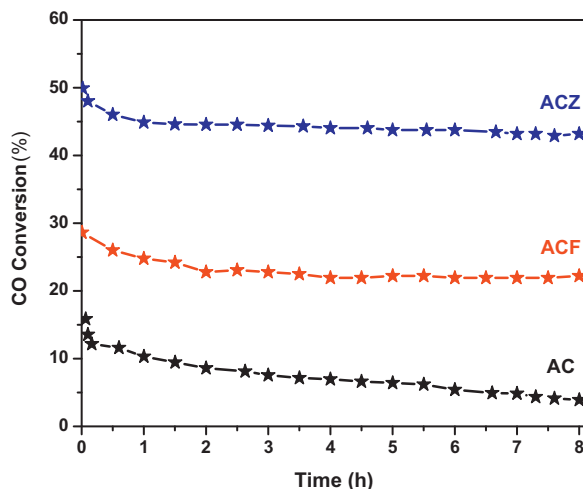


Fig. 10. Stability of CO oxidation activity over Au/CeO₂ (AC), Au/CeO₂-Fe₂O₃ (ACF), and Au/CeO₂-ZrO₂ (ACZ) catalysts studied at 328 K.

particles with diameter of below 5 nm exhibit high catalytic activity in comparison to large Au particles (20–40 nm). It is noticed from the XRD and TEM studies that doped ceria supports show a favorable effect toward gold particle size. However, the AC catalyst exhibited higher CO oxidation activity than the ACL sample. Therefore, it can be presumed that the presence of small Au particles is not the only prerequisite for achieving high CO conversion [12,51,52]. The oxidation state of gold also plays a crucial role in the CO oxidation: indeed there is a sturdy controversy about this subject [52,53]. It was reported that oxidized or partially oxidized gold serves as a key species in the CO oxidation. Conversely, many studies proposed that metallic gold (Au⁰) particles are the main catalytically active species. In the particular case of Au/CeO₂, the metallic gold species shows better CO oxidation activity when compared to ionic gold [54,55]. In the present study, all the gold samples exhibited only Au⁰ species (evidence from XPS results, Fig. 4). Therefore, it can be suggested that the metallic Au species alone catalyze CO oxidation at quite low temperatures in the absence of ionic Au species.

It has been proved that the existence of oxygen vacancies in the ceria supports shows a beneficial effect toward the gold dispersion, leading to smaller gold particles and thereby, enhanced CO oxidation activity [9,56,57]. As we mentioned earlier, the Au/doped-CeO₂ catalysts exhibited smaller Au NPs due to the presence of larger amounts of oxygen vacancies in the doped ceria supports. Moreover, the activation of oxygen during CO oxidation mainly occurs on the surface of oxygen vacancies in the vicinity of the boundary with the gold particles [58,59]. The activated oxygen reacts with an adjacent CO molecule adsorbed on gold most likely at the edges and the corners. As well-known, the formation of oxygen vacancies is accompanied by the reduction of Ce⁴⁺ ions to Ce³⁺, and the concentration of Ce³⁺ ions is proportional to that of oxygen vacancies [60]. Among the studied catalysts, the ACZ sample exhibited higher concentration of Ce³⁺ ions (Table 3), and hence, it contains a large amount of oxygen vacancies. The promotional effect of Ce³⁺ ions is noticed for CO oxidation of Au/CeO₂ catalysts [47,61,62]. Therefore,

the existence of enriched Ce³⁺ ions and thereby, improved oxygen vacancies could be a reason for the higher CO oxidation activity of the ACZ catalyst in comparison to other Au catalysts. Although the ACL catalyst has a large amount of Ce³⁺ ions compared to AC sample (Table 3), it showed very low CO oxidation activity.

Several experimental studies have proved that existence of carbonate species on the surface of Au catalysts could block the active sites essential for CO oxidation [63–66]. The accumulation of carbonates strongly depends on the nature of the support. The acidic supports were found to be more resistant to deactivation by carbonates than the basic supports [67]. Generally, ceria is characterized by both acidic- and basic-properties, which can be significantly improved by doping of various metal ions [68–70]. Consequently, they can be easily hydroxylated and/or carbonated in the presence of air. In particular, CO₂ (a weak Lewis acid) is an unavoidable contaminant of ceria-based materials [71]. To understand this, the un-calcined gold catalysts were subjected to TG-DTA analysis as shown in Fig. 11. All samples exhibited a strong endothermic peak between 323 and 423 K, indicating desorption of either physically or chemically adsorbed water molecules [71,72]. Additionally, an endothermic peak was identified at around 573 K for the AC, ACZ and ACF samples attributed to desorption of more firmly bounded carbonate species [71,73,74]. Therefore, it is understandable that thermal treatment of these catalysts at 573 K efficiently removes the surface carbonates. On the contrary, the ACL catalyst exhibited several weight loss peaks at higher temperatures due to the removal of different hydroxycarbonate and/or polycarbonate species, and other contaminants [71]. Therefore, most of the carbonates would be retained on the surface of the ACL catalyst after calcination at 573 K. The ability of ACL catalyst to form various carbonates is due to the strong basic nature of the La as compared to Zr and Fe (acidic nature) [75–77]. Hence, it can be expected that incorporation of Zr and Fe enhances the acidic properties of CeO₂, whereas the La-doping improves the basic properties.

To know the effect of La on the acid-base properties of the CeO₂, we have performed TPD of NH₃ and of CO₂ over the CL support (Fig. S5 of the supplementary material). The NH₃-TPD profile shows three desorption maxima at around 424, 673 and 972 K, corresponding to weak, medium and strong acidic sites, respectively [78]. Similar to NH₃-TPD, in the CO₂-TPD profiles also, three peaks could be observed at around 395, 723 and 997 K, respectively, related to weak, medium and strong basic sites. The estimated relative ratio of basic sites to acidic sites (B/A~71.2%) reveals that the CL support exhibits higher concentration of basic sites than of acidic sites. Therefore, it can be expected that the ACL catalyst has strong ability to form and/or adsorb different carbonate species, which could be the reason for its low CO oxidation activity. In addition, due to strong carbonate adsorption ability of ACL catalyst, the formed CO₂ in the CO oxidation reaction could interact with the surface active sites that facilitate the generation of more carbonate species [79]. The resultant carbonates would remain on the catalyst surface and the reaction temperatures are high enough for the decomposition of carbonates, leading to the unusual enhancement in the catalytic activity. As stated, the observed sharp increase in the CO oxidation of ACL sample might be due to desorption of the accumulated carbonate species. These interesting findings could be

Table 3

XPS core level binding energies of gold, cerium, oxygen and dopants in the synthesized gold catalysts.

| Sample | Au 4f _{7/2} (eV) | O 1s (eV) | Ce 3d _{5/2} (eV) | Zr 3d _{5/2} (eV) | La 3d _{5/2} (eV) | Fe 2p _{3/2} (eV) | I _u /I _{Total} ^a |
|--------|---------------------------|-----------|---------------------------|---------------------------|---------------------------|---------------------------|--|
| AC | 83.6 | 528.8 | 917.5 | – | – | – | 0.0896 |
| ACZ | 83.5 | 529.4 | 916.7 | 182.3 | – | – | 0.0625 |
| ACL | 83.5 | 529.7 | 916.6 | – | 834.4 | – | 0.0713 |
| ACF | 83.3 | 529.4 | 917.1 | – | – | 711.2 | 0.0876 |

^a Estimated from the Ce 3d XPS spectra.

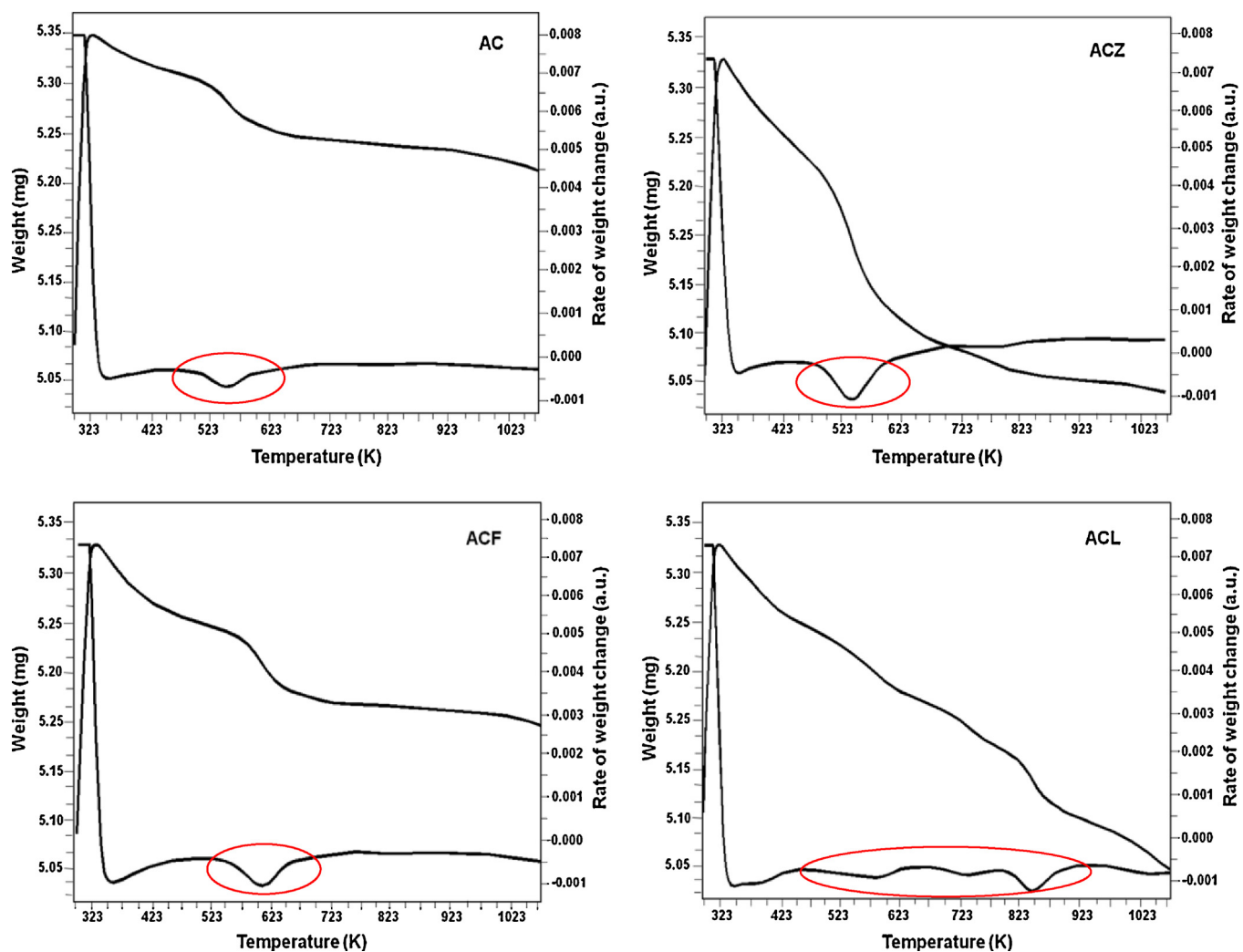


Fig. 11. TG-DTA profiles of Au/CeO₂ (AC), Au/CeO₂-Fe₂O₃ (ACF), Au/CeO₂-La₂O₃ (ACL) and Au/CeO₂-ZrO₂ (ACZ) catalysts.

helpful in the development of doped-CeO₂ supported Au catalysts for CO oxidation and related applications.

4. Conclusions

The modification of CeO₂ was successfully achieved by incorporation of various metal ions, namely Fe³⁺, La³⁺ and Zr⁴⁺. Doped ceria samples exhibited smaller crystallite size, higher specific surface area and more abundant oxygen vacancies than pure ceria. Among, Zr-incorporation showed a favorable role on the textural properties of ceria. The XRD and TEM analyses revealed the promotional role of dopants to obtain smaller gold nanoparticles. Among the investigated catalysts, the Au/CeO₂-ZrO₂ catalyst exhibited the highest CO oxidation activity, which was attributed to its high content of Ce³⁺ ions and oxygen vacancies. On the other hand, the La-doped Au/CeO₂ showed an opposite effect because of its strong ability to form and/or adsorb various carbonates, which could block the active sites crucial for CO oxidation. Further, the ACZ and ACF catalysts exhibited reasonably stable activity in the time-on-stream studies in comparison to the AC catalyst.

Acknowledgments

We thank DST (India) and DAAD (Germany) for financial support under a bilateral collaboration program (DST-DAAD-PPP-2010).

P.S., B.M., and P.S.R. thank Council of Scientific and Industrial Research, New Delhi, for the award of research fellowships.

Appendix A. Supplementary data

Supplementary material related to this article can be found, in the online version, at <http://dx.doi.org/10.1016/j.apcatb.2013.08.035>.

References

- [1] Z. Ma, S. Dai, *Nano Research* 4 (1) (2011) 3–32.
- [2] L.M. Martínez, T.F. Romero-Sarria, W.Y. Hernández, M.A. Centeno, J.A. Odriozola, *Applied Catalysis A: General* 423–424 (2012) 137–145.
- [3] S.A.C. Carabineiro, N. Bogdanchikova, P.B. Tavares, J.L. Figueiredo, *RSC Advances* 2 (2012) 2957–2965.
- [4] W.G. Menezes, V. Zielašek, K. Thiel, A. Hartwig, M. Bäumer, *Journal of Catalysis* 299 (2013) 222–231.
- [5] S. Yong-an, S. Yue-nian, J. Mei-lin, G. Jin-ling, *Chemical Research in Chinese Universities* 26 (2010) 453–459.
- [6] M. Stratakis, H. Garcia, *Chemical Reviews* 112 (2012) 4469–4506.
- [7] A. Longo, L.F. Liotta, G. Pantaleo, F. Giannici, A.M. Venezia, A. Martorana, *Journal of Physical Chemistry C* 116 (2012) 2960–2966.
- [8] A. Longo, L.F. Liotta, G. Di Carlo, F. Giannici, A.M. Venezia, A. Martorana, *Chemistry of Materials* 22 (2010) 3952–3960.
- [9] G. Avgouropoulos, M. Manzoli, F. Bocuzzi, T. Tabakova, J. Papavasiliou, T. Ioannides, V. Idakiev, *Journal of Catalysis* 256 (2008) 237–247.
- [10] S. Ivanova, V. Pitchon, C. Petit, *Journal of Molecular Catalysis A: Chemical* 256 (2006) 278–283.

- [11] S.A. Jimenez-Lam, M.G. Cardenas-Galindo, B.E. Handy, S.A. Gomez, G.A. Fuentes, J.C. Fierro-Gonzalez, *Journal of Physical Chemistry C* 115 (2011) 23519–23526.
- [12] A.M. Venezia, G. Pantaleo, A. Longo, G. Di Carlo, M.P. Casaleotto, F.L. Liotta, G. Deganello, *Journal of Physical Chemistry B* 109 (2005) 2821–2827.
- [13] B.M. Reddy, G. Thrimurthulu, L. Katta, Y. Yamada, S.-E. Park, *Journal of Physical Chemistry C* 113 (2009) 15882–15890.
- [14] B.M. Reddy, L. Katta, G. Thrimurthulu, *Chemistry of Materials* 22 (2010) 467–475.
- [15] T. Masui, Y. Peng, K. Machida, G. Adachi, *Chemistry of Materials* 10 (1998) 4005–4009.
- [16] R. Si, Y.-W. Zhang, L.-M. Wang, S.-J. Li, B.-X. Lin, W.-S. Chu, Z.-Y. Wu, C.-H. Yan, *Journal of Physical Chemistry C* 111 (2007) 787–794.
- [17] S. Damyanova, B. Pawelec, K. Arishtirova, M.V. Martinez Huerta, J.L.G. Fierro, *Applied Catalysis A: General* 337 (2008) 86–96.
- [18] O.H. Laguna, F. Romero-Sarria, M.A. Centeno, J.A. Odriozola, *Journal of Catalysis* 276 (2010) 360–370.
- [19] C. Liang, Z. Ma, H. Lin, L. Ding, J. Qiu, W. Frandsen, D. Su, *Journal of Materials Chemistry* 19 (2009) 1417–1424.
- [20] Y. Zuo, X. Huang, L. Li, G. Li, *Journal of Materials Chemistry A* 1 (2013) 374–380.
- [21] J.D. Lessard, I. Valsamakis, M. Flytzani-Stephanopoulos, *Chemical Communications* 48 (2012) 4857–4859.
- [22] S. Ivanova, V. Pitchon, Y. Zimmermann, C. Petit, *Applied Catalysis A: General* 298 (2006) 57–64.
- [23] L. Katta, P. Sudarsanam, B. Mallesham, B.M. Reddy, *Catalysis Science & Technology* 2 (2012) 995–1004.
- [24] L. Katta, P. Sudarsanam, G. Thrimurthulu, B.M. Reddy, *Applied Catalysis B: Environmental* 101 (2010) 101–108.
- [25] D. Hari Prasad, S.Y. Park, H.I. Ji, H.R. Kim, J.W. Son, B.K. Kim, H.W. Lee, J.H. Lee, *Journal of Physical Chemistry C* 116 (2012) 3467–3476.
- [26] L. Li, G. Li, Y. Che, W. Su, *Chemistry of Materials* 12 (2000) 2567–2574.
- [27] O.H. Laguna, M.A. Centeno, M. Boutonnet, J.A. Odriozola, *Applied Catalysis B: Environmental* 106 (2011) 621–629.
- [28] M.M. Wang, L. He, Y.M. Liu, Y. Cao, H.Y. He, K.N. Fan, *Green Chemistry* 13 (2011) 602–607.
- [29] W. Yan, B. Chen, S.M. Mahurin, V. Schwartz, D.R. Mullins, A.R. Lupini, S.J. Pennycook, S. Dai, S.H. Overbury, *Journal of Physical Chemistry B* 109 (2005) 10676–10685.
- [30] L.F. Liotta, G. Di Carlo, G. Pantaleo, A.M. Venezia, *Catalysis Today* 158 (2010) 56–62.
- [31] X. Zhang, H. Shi, B.Q. Xu, *Journal of Catalysis* 279 (2011) 75–87.
- [32] M. Ousmane, L.F. Liotta, G. Di Carlo, G. Pantaleo, A.M. Venezia, G. Deganello, L. Retailleau, A. Boreave, A. Giroir-Fendler, *Applied Catalysis B: Environmental* 101 (2011) 629–637.
- [33] G.J. Hutchings, M.S. Hall, A.F. Carley, P. Landon, E. Benjamin, C.J. Solsona, A. Kiely, M. Herzing, J.A. Makkee, A. Mouljin, J.C. Overweg, J. Fierro-Gonzalez, B.C. Guzman, Gates, *Journal of Catalysis* 242 (2006) 71–81.
- [34] L. Katta, B.M. Reddy, M. Muhler, W. Grunert, *Catalysis Science & Technology* 2 (2012) 745–753.
- [35] G.N. Vayssiolov, M. Mihaylov, St.P. Petkov, K.I. Hadjiivanov, K.M. Neyman, *Journal of Physical Chemistry C* 115 (2011) 23435–23454.
- [36] Y. Zhou, J. Zhou, *Journal of Physical Chemistry Letters* 1 (2010) 1714–1720.
- [37] J. He, G.K. Reddy, S.W. Thiel, P.G. Smirniotis, N.G. Pinto, *Journal of Physical Chemistry C* 115 (2011) 24300–24309.
- [38] X.-S. Huang, H. Sun, L.-C. Wang, Y.-M. Liu, K.-N. Fan, Y. Cao, *Applied Catalysis B: Environmental* 90 (2009) 224–232.
- [39] J. Wang, S. Yina, M. Komatsua, T. Sato, *Journal of the European Ceramic Society* 25 (2005) 3207–3212.
- [40] T. Yamashita, P. Hayes, *Applied Surface Science* 254 (2008) 2441–2449.
- [41] A. Karpenko, R. Leppelt, J. Cai, V. Plzak, A. Chuvilin, U. Kaiser, R.J. Behm, *Journal of Catalysis* 250 (2007) 139–150.
- [42] S. Anandan, N. Pugazhenthiran, T. Selvamani, S.-H. Hsieh, G.-J. Lee, J.J. Wu, *Catalysis Science & Technology* 2 (2012) 2502–2507.
- [43] J.T. Carneiro, T.J. Savenije, G. Mul, *Physical Chemistry Chemical Physics* 11 (2009) 2708–2714.
- [44] Y.-B. Tu, J.-Y. Luo, M. Meng, G. Wang, J.-J. He, *International Journal of Hydrogen Energy* 34 (2009) 3743–3754.
- [45] Z. Chen, Q. Gao, *Applied Catalysis B: Environmental* 84 (2008) 790–796.
- [46] G.R. Rao, H.R. Sahu, *Proceedings of the Indian Academy of Sciences (Journal of Chemical Sciences)* 113 (2001) 651–658.
- [47] H.Y. Kim, G. Henkelman, *Journal of Physical Chemistry Letters* 4 (2013) 216–221.
- [48] H.Y. Kim, G. Henkelman, *Journal of Physical Chemistry Letters* 3 (2012) 2194–2199.
- [49] K. Liu, A. Wang, T. Zhang, *ACS Catalysis* 2 (2012) 1165–1178.
- [50] B.K. Min, C.M. Friend, *Chemical Reviews* 107 (2007) 2709–2724.
- [51] K. Qian, S. Lv, X. Xiao, H. Sun, J. Lu, M. Luo, W. Huang, *Journal of Molecular Catalysis A: Chemical* 306 (2009) 40–47.
- [52] S.A.C. Carabineiro, S.S.T. Bastos, J.J.M. Órfao, M.F.R. Pereira, J.J. Delgado, J.L. Figueiredo, *Applied Catalysis A: General* 381 (2010) 150–160.
- [53] S.A.C. Carabineiro, A.M.T. Silva, G. Drazic, P.B. Tavares, J.L. Figueiredo, *Catalysis Today* 154 (2010) 21–30.
- [54] M. Manzoli, G. Avgoustopoulos, T. Tabakova, J. Papavasiliou, T. Ioannides, F. Bocuzzi, *Catalysis Today* 138 (2008) 239–243.
- [55] N. Hickey, P.A. Laroche, C. Gentilini, L. Sordelli, L. Olivi, S. Polizzi, T. Montini, P. Fornasiero, L. Pasquato, M. Graziani, *Chemistry of Materials* 19 (2007) 650–651.
- [56] O.H. Laguna, M.A. Centeno, F. Romero-Sarria, J.A. Odriozola, *Catalysis Today* 172 (2011) 118–123.
- [57] M.I. Domínguez, F. Romero-Sarria, M.A. Centeno, J.A. Odriozola, *Applied Catalysis B: Environmental* 87 (2009) 245–251.
- [58] M. Haruta, *Faraday Discussions* 152 (2011) 11–32.
- [59] L. Ilieva, G. Pantaleo, I. Ivanov, R. Zanella, A.M. Venezia, D. Andreeva, *International Journal of Hydrogen Energy* 34 (2009) 6505–6515.
- [60] H.Y. Kim, H.M. Lee, G. Henkelman, *Journal of the American Chemical Society* 134 (2012) 1560–1570.
- [61] A. Horvath, A. Beck, G. Stefler, T. Benko, G. Safran, Z. Varga, J. Gubicza, L. Guczi, *Journal of Physical Chemistry C* 115 (2011) 20388–20398.
- [62] L. Escamilla-Perea, R. Nava, B. Pawelec, M.G. Rosmaninho, C.L. Peza-Ledesma, J.L.G. Fierro, *Applied Catalysis A: General* 381 (2010) 42–53.
- [63] F.C. Meunier, D. Reid, A. Goguet, S. Shekhtman, C. Hardacre, R. Burch, W. Deng, M. Flytzani-Stephanopoulos, *Journal of Catalysis* 247 (2007) 277–287.
- [64] X. Bokhimi, R. Zanella, A. Morales, V. Maturano, C. Ángeles-Chávez, *Journal of Physical Chemistry C* 115 (2011) 5856–5862.
- [65] S.H. Oh, G.B. Hoflund, *Journal of Physical Chemistry A* 110 (2006) 7609–7613.
- [66] D. Widmann, Y. Liu, F. Schüth, R.J. Behm, *Journal of Catalysis* 276 (2010) 292–305.
- [67] L. Ilieva, G. Pantaleo, I. Ivanov, R. Zanella, J.W. Sobczak, W. Lisowski, A.M. Venezia, D. Andreeva, *Catalysis Today* 175 (2011) 411–419.
- [68] M.C.I. Bezen, C. Breitkopf, N. El Kolla, J.-M. Krafft, C. Louis, J.A. Lercher, *Chemistry – A European Journal* 17 (2011) 7095–7104.
- [69] S. Mandal, K.K. Bando, C. Santra, S. Maity, O.O. James, D. Mehta, B. Chowdhury, *Applied Catalysis A: General* 452 (2013) 94–104.
- [70] S. Mandal, C. Santra, K.K. Bando, O.O. James, S. Maity, D. Mehta, B. Chowdhury, *Journal of Molecular Catalysis A: Chemical* 378 (2013) 47–56.
- [71] B. Azambre, S. Collura, P. Darcy, J.M. Trichard, P. Da Costa, A. García-García, A. Bueno-López, *Fuel Processing Technology* 92 (2011) 363–371.
- [72] J.L. Cao, Y. Wang, T.Y. Zhang, S.H. Wu, Z.Y. Yuan, *Applied Catalysis B: Environmental* 78 (2008) 120–128.
- [73] G. Colón, J.A. Navío, R. Monaci, I. Ferino, *Physical Chemistry Chemical Physics* 2 (2000) 4453–4459.
- [74] R.V. Wandekar, B.N. Wani, S.R. Bharadwaj, *Solid State Sciences* 11 (2009) 240–250.
- [75] F. Vindigni, M. Manzoli, T. Tabakova, V. Idakiev, F. Bocuzzi, A. Chiorino, *Applied Catalysis B: Environmental* 125 (2012) 507–515.
- [76] G. Neri, A. Bonavita, G. Rizzo, S. Galvagno, S. Capone, P. Siciliano, *Sensors and Actuators B* 114 (2006) 687–695.
- [77] M. Mihaylov, E. Ivanova, Y. Hao, K. Hadjiivanov, H. Knözinger, B.C. Gates, *Journal of Physical Chemistry C* 112 (2008) 18973–18983.
- [78] P.S. Reddy, P. Sudarsanam, G. Raju, B.M. Reddy, *Journal of Industrial and Engineering Chemistry* 18 (2012) 648–654.
- [79] F. Romero-Sarria, M.I. Domínguez, M.A. Centeno, J.A. Odriozola, *Applied Catalysis B: Environmental* 107 (2011) 268–273.